Reconfigurable neural spiking in bias field free spin Hall nano-oscillator

Sourabh Manna,[1] Rohit Medwal,[2] and Rajdeep Singh Rawat[1,*]
[1]*Natural Sciences and Science Education, National Institute of Education, Nanyang Technological University, Singapore 637616, Singapore*
[2]*Department of Physics, Indian Institute of Technology Kanpur, Kanpur, Uttar Pradesh 208016, India*

(Received 11 September 2023; revised 24 October 2023; accepted 24 October 2023; published 14 November 2023)

In this paper, we theoretically investigate neuronlike spiking dynamics in an elliptic ferromagnet (FM)/heavy metal bilayer-based spin Hall nano-oscillator (SHNO) in a bias field free condition, very suitable for practical realization of brain-inspired computing schemes. We demonstrate regular periodic spiking with tunable frequency as well as the leaky integrate-and-fire (LIF) behavior in a single SHNO by manipulating the pulse features of input current. The frequency of regular periodic spiking is tunable in a range of 0.5–0.96 GHz (460 MHz bandwidth) through adjusting the magnitude of constant input DC current density. We further demonstrate the reconfigurability of spiking dynamics in response to a time-varying input accomplished by continuously increasing the input current density as a linear function of time. Macrospin theory and micromagnetic simulation provide insight into the origin of bias field free auto-oscillation and the spiking phenomena in our SHNO. In addition, we discuss how the shape anisotropy of the elliptic FM influence the bias field free auto-oscillation characteristics, including threshold current, frequency, and transition from in-plane to out-of-plane precession. The SHNO operates $<10^{12}$ A/m^2 input current density and exhibits a large auto-oscillation amplitude, ensuring high output power. We show that the threshold current density can be reduced by decreasing the ellipticity of the FM layer as well as enhancing the perpendicular magnetic anisotropy. These findings highlight the potential of bias field free elliptic SHNO in designing power-efficient spiking neuron-based neuromorphic hardware.

DOI: 10.1103/PhysRevB.108.184411

I. INTRODUCTION

The pursuit of more efficient brain-inspired computing systems drives us to explore beyond-conventional computing paradigms, including neuromorphic and reservoir computing [1–3], for machine learning and artificial intelligence (AI) applications. Neuromorphic hardware employs artificial neurons to emulate the spiking dynamics observed in biological neural networks. Consequently, the spiking neural network (SNN), composed of multiple neuronlike software units, seamlessly integrates with the energy-efficient architectures of neuromorphic hardware due to its sparse event-driven processing. Several neuromorphic computing approaches abstract neurons as nonlinear oscillators [4–6]. Spintronic oscillators are highly suitable for realization of scalable SNN-based neuromorphic hardware because of their nanoscale size and inherent nonlinearity. Spin-torque nano-oscillators (STNOs) and spin Hall nano-oscillators (SHNOs) have already emerged as efficient candidates for performing various classification and combinatorial optimization tasks [7–13]. In addition, spiking dynamics have been realized in STNO and SHNO devices through several methods such as anisotropy variation in ferromagnetic (FM) layers [6,14], excitation of nonuniform sublattice-magnetization dynamics in easy-plane antiferromagnets (AFMs) [15,16], voltage pulse-induced stimulation with an injection lock-in mechanism [17], and nonlinear magnon generation via excitation with a microwave field [18]. Particularly SHNO devices, relying on the spin Hall effect [19] to generate spin-orbit torque (SOT), are growing in interest because of their easy fabrication process, miniature footprint, lower Joule heating, and robust nonlinear magnetization dynamics [20–27]. In addition, recently demonstrated bias field free operation of a SHNO has expanded its applicability for designing low-power AI hardware [28–31]. Marković *et al.* [32] have demonstrated state-of-the-art neuronlike spiking dynamics in an easy-plane FM/heavy metal (HM)-based nanoconstriction SHNO that can potentially enable unsupervised learning. Typically, in a spiking SHNO, application of short nanosecond current pulses triggers the spiking behavior in magnetization dynamics. However, a regular periodic spiking induced by a constant dc input current, such as Huxley-Hodgkin spikes [33], has not been observed in a FM/HM bilayer SHNO.

In most SNNs, the leaky integrate-and-fire (LIF) feature of biological neurons is employed due to its simplicity, enabling easier hardware implementation and large-scale integration. Although the LIF behavior has been demonstrated through domain wall motion [34], magnetization auto-oscillation in synthetic AFM heterostructure [14] and skyrmion dynamics [35], it remains unexplored in bias field free SHNO devices. In this paper, we demonstrate both the regular periodic spiking and LIF behavior in a single FM/HM bilayer SHNO, consisting of an elliptical FM interfaced with a rectangular HM

*Corresponding author: rajdeep.rawat@nie.edu.sg

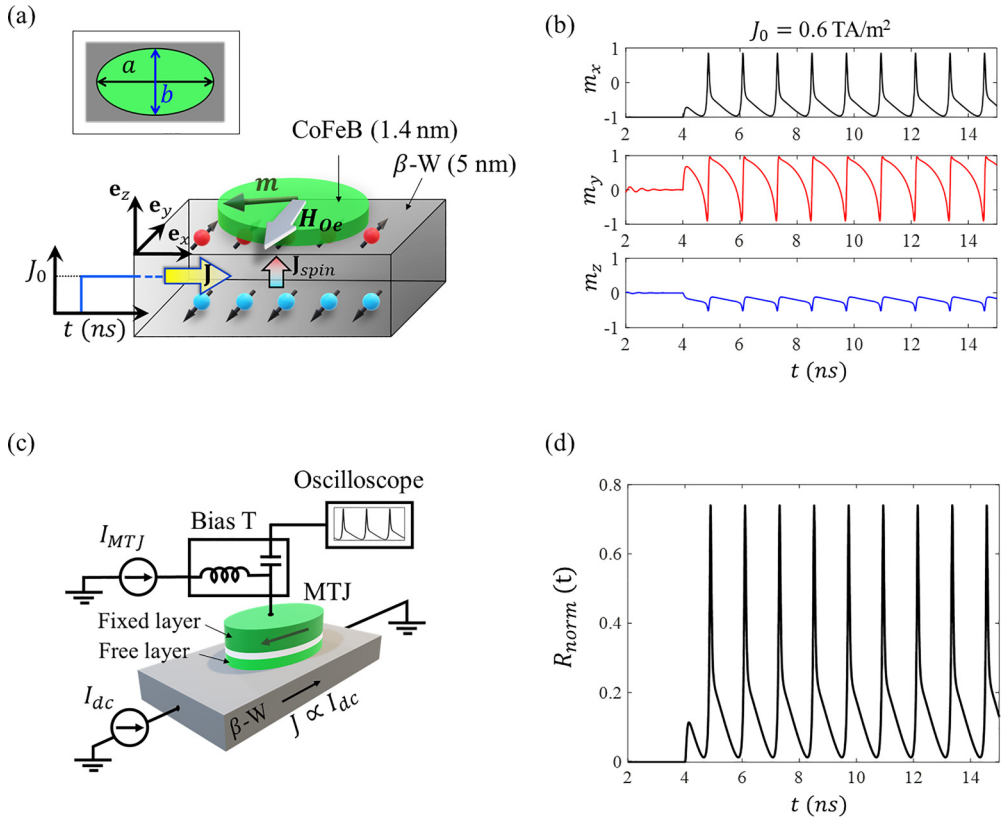

FIG. 1. (a) Schematic illustration of the spin Hall nano-oscillator (SHNO) device. $\mathbf{e}_x$, $\mathbf{e}_y$, and $\mathbf{e}_z$ denote the unit vectors along x, y, and z axes, respectively. (Inset) top view of the elliptic ferromagnet (FM). (b) Time evolution of the components of normalized magnetization $\mathbf{m}$ for input current density $J_0 = 0.6\,\mathrm{TA/m^2}$. (c) Schematic of the proposed electrical circuit for detection of auto-oscillation and spiking dynamics using the tunneling magnetoresistance (TMR) of a magnetic tunnel junction (MTJ). The free layer of the MTJ represents the FM layer of (a). (d) Time evolution of the normalized TMR corresponding to the variation of $\mathbf{m}$ in (b), calculated using 80% TMR ratio.

layer in bias field free condition. We comprehensively investigate the underlying mechanism responsible for the bias field free auto-oscillation of magnetization and subsequent spiking phenomena. The simple elliptic geometry enables precise analytical calculation of demagnetization coefficients [36]. Consequently, we explore the role of a shape-dependent demagnetization field in the presence of perpendicular magnetic anisotropy (PMA) in an elliptical SHNO, which is essential to optimize the device geometry for achieving higher output power, improved tunability, and enhanced quality of the spikes.

The paper is structured as follows: It begins with the detailed micromagnetic simulation methodology of an elliptic SHNO system. Exploring bias-free auto-oscillation characteristics, we reveal the in-plane (IP) to out-of-plane (OOP) transition in magnetization precession. A macrospin model then elucidates the origin of bias field free auto-oscillation in an elliptical SHNO and how it is influenced by the shape anisotropy of the FM layer. Moving on, the SOT-induced spiking behavior in the OOP precession mode is demonstrated. This is followed by the investigation of how the demagnetization field determines the spiking rate and quality (sharpness of the spikes) in our system. Finally, the LIF behavior along with the reconfigurable spiking in response to variable input current is demonstrated, highlighting the potential of bias field free SHNOs in neuromorphic hardware design.

II. MICROMAGNETIC SIMULATION OF BIAS FIELD FREE SHNO

We designed an SHNO device consisting of a 1.4-nm-thin elliptic FM (CoFeB) layer interfaced with a rectangular 5-nm-thick layer of HM (β-W), as shown in Fig. 1(a). We have chosen β-W as the HM layer because of its high spin Hall angle [24,37,38]. The lateral dimension of the β-W layer is large enough as compared with the major and minor axes of the elliptic CoFeB layer. Therefore, the Oersted field generated upon passing a charge current through the β-W layer is uniform and unidirectional over the CoFeB layer. The major and minor axes of the elliptic CoFeB layer are denoted by a and b, respectively, as shown in the inset of Fig. 1(a). We also define the axis ratio as $r = a/b$. Note that all the results presented in this paper are obtained for $r = 3$ unless mentioned otherwise. A Cartesian coordinate system is defined with the x axis parallel to the major axis and the y axis parallel to the minor axis of the ellipse, whereas the z axis is normal to the plane of the ellipse, as shown in Fig. 1(a).

The material parameters chosen from experiments in Ref. [24] are as follows: The CoFeB layer ($Co_{20}Fe_{60}B_{20}$) has a saturation magnetization $M_s = 740$ kA/m, exchange constant $A_{ex} = 19$ pJ/m, damping constant $\alpha = 0.023$, PMA field $H_{PMA} = 0.57$ T, and gyromagnetic ratio $\gamma = 1.879 \times 10^{11}$Hz/T. Note that H_{PMA} is not sufficient to overcome the

OOP demagnetization field ($\sim\mu_0 M_s = 0.93$ T). Therefore, the equilibrium magnetization resides in the xy plane in the absence of SOT. However, the substantial $H_{\rm PMA}$ helps in exciting the magnetization auto-oscillation by reducing the effective OOP demagnetization field. The spin Hall angle of β-W has been chosen as $\theta_{\rm SH} = -0.41$. A charge current density $\mathbf{J}$ along the x axis passing through the β-W layer generates a transverse spin current polarized along the y direction. Injection of this spin current into the FM CoFeB layer exerts a dampinglike SOT (DLT) on the magnetization that counters the damping torque. Note that the SOT includes a fieldlike torque (FLT) as well in addition to the dampinglike torque in general. However, the FLT in the CoFeB/β-W system is negligible as compared with the DLT [39]. Therefore, we consider only the DLT in the Slonczewski form [40]. The input charge current induces an Oersted field given as $\mathbf{H}_{\rm Oe} = -\frac{\mu_0 |\mathbf{J}| t_{\rm HM}}{2}\mathbf{e}_y$, where $t_{\rm HM}$ denotes the thickness of the HM layer and $\mathbf{e}_y$ denotes the unit vector along the y axis. The Oersted field allows the magnetization to orient slightly away from the x axis in a relaxed state, which breaks the orthogonality of equilibrium magnetization and the spin-polarization direction $\mathbf{p} = \mathbf{e}_y$. We emphasize that no external biasing magnetic field has been considered. The magnetization dynamics of the CoFeB layer can then be expressed in terms of the reduced magnetization $\mathbf{m} = \mathbf{M}/M_s$, following the Landau-Lifshitz-Gilbert-Slonczewski equation as [40,41]

$$\dot{\mathbf{m}} = -\gamma \mathbf{m} \times \mathbf{H}_{\rm eff} + \alpha \mathbf{m} \times \dot{\mathbf{m}} + \frac{\gamma |\mathbf{J}| \hbar \theta_{\rm SH}}{2 e t_{\rm FM} \mu_0 M_s} \mathbf{m} \times (\mathbf{p} \times \mathbf{m}). \tag{1}$$

In Eq. (1), $\mathbf{H}_{\rm eff} = (\mathbf{H}_{\rm Oe} + \mathbf{H}_{\rm ex} + \mathbf{H}_{\rm dem} + \mathbf{H}_{\rm PMA})$, where $\mathbf{H}_{\rm ex}$, $\mathbf{H}_{\rm dem}$, and $\mathbf{H}_{\rm PMA}$ denote the exchange, demagnetization, and the PMA fields, respectively. The constants e, $\hbar$, $t_{\rm FM}$, and μ_0 represent the magnitude of electronic charge, reduced Planck's constant, thickness of the FM layer, and permeability of free space, respectively.

We have quantitatively obtained the dynamic behavior of magnetization by numerically solving Eq. (1), using the open-source GPU accelerated software MuMax^3 [42]. In the simulation, the dc charge current is switched on after 4 ns (i.e., $|\mathbf{J}| = 0$ for $t \leqslant 4$ ns and $|\mathbf{J}| = J_0$ for $t > 4$ ns). This delay allows the magnetization to completely relax and reach a stable state before the SOT starts acting on it [see Fig. 1(a)]. Figure 1(b) shows the time evolution of the components of $\mathbf{m}$ ($\mathbf{m} = m_x\mathbf{e}_x + m_y\mathbf{e}_y + m_z\mathbf{e}_z$) for an input current density $J_0 = 0.6\,\mathrm{TA/m^2}$ in the case of $r = 3$. As seen from Fig. 1(b), the magnetization undergoes sustained auto-oscillation which generates periodic spiking in m_x, m_y, and m_z. However, the spiking amplitude is much more prominent in m_x and m_y than m_z, denoting the magnetization precession about a highly OOP axis. In addition, we observe that the amplitude of auto-oscillation is very large in the xy plane which ensures high output power from this bias field free SHNO. The generation of auto-oscillation and subsequent spiking process are discussed in detail in later sections. The spikes in m_x can be easily recorded as voltage signal using the tunneling magnetoresistance (TMR) of a magnetic tunnel junction (MTJ) and implementing the circuit shown in Fig. 1(c). The TMR pillar can be designed such that the FM layer adjacent to the HM is the free layer, and the top FM layer is the fixed layer with magnetization oriented along the major axis of ellipse. The shape anisotropy of the elliptical fixed layer favors this orientation of magnetization. Hence, no extra AFM layer would be required for pinning the magnetization in the fixed layer. The TMR voltage is given as $V = I_{\rm MTJ} \times R_{\rm MTJ}$, where $R_{\rm MTJ}$ is the resistance across the MTJ. We define the normalized $R_{\rm MTJ}$ as [6]

$$R_{\rm norm} = \frac{r_{TMR}(1 + m_x)}{2}. \tag{2}$$

Here, $r_{\rm TMR}$ denotes the TMR ratio given by $r_{\rm TMR} = (R^{\uparrow\downarrow}_{\rm MTJ} - R^{\uparrow\uparrow}_{\rm MTJ})/R^{\uparrow\uparrow}_{\rm MTJ}$. Considering a typical MTJ with 80% TMR, we calculate the time evolution of the normalized TMR $R_{\rm norm}$ [see Fig. 1(d)] which shows the periodic spiking behavior as observed in $m_x(t)$.

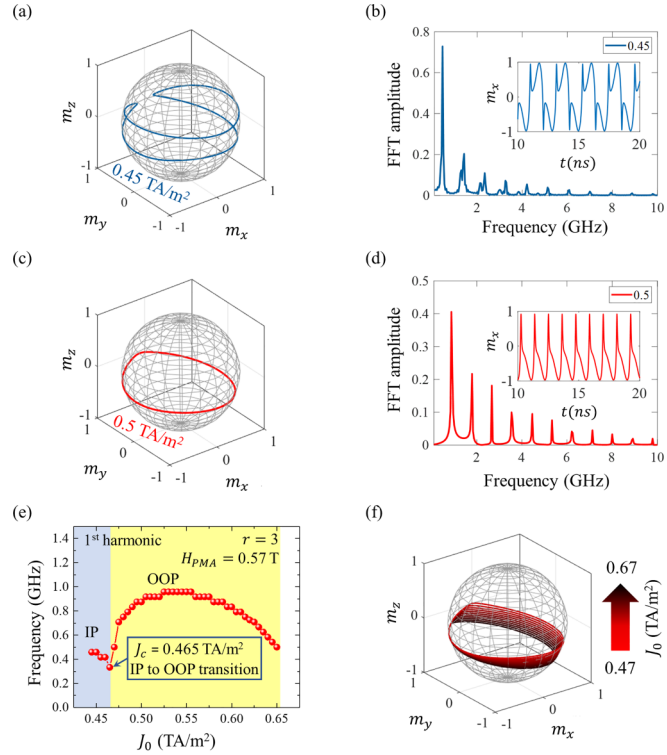

FIG. 2. (a) Trajectory of the steady state magnetization precession for $J_0 = 0.45\,\mathrm{TA/m^2}$ and (b) the corresponding FFT of $m_x(t)$. Similar plots for a higher current density $J_0 = 0.5\,\mathrm{TA/m^2}$ are shown in (c) and (d). The magnetization precession in (a) and (c) represents the in-plane (IP) and out-of-plane (OOP) precession modes, respectively. (e) Variation of the first harmonic of the auto-oscillation frequency as a function of input current density J_0, showing the IP to OOP transition in precession mode. (f) Steady-state trajectories of OOP precession mode for input current density ranging from 0.45 to $0.67\,\mathrm{TA/m^2}$.

III. CHARACTERISTICS OF THE AUTO-OSCILLATION

Looking into the auto-oscillation characteristics, we find that the spiking behavior is not present right from the onset of auto-oscillation. In fact, at lower current density, the magnetization undergoes auto-oscillation about an IP precession axis. Figure 2(a) shows the trajectory of $\mathbf{m}$ in such a typical IP precession mode for $J_0 = 0.45\,\mathrm{TA/m^2}$. The corresponding

fast Fourier transform (FFT) of $m_x(t)$ in Fig. 2(b) shows the presence of several harmonics, although the first harmonic is relatively much stronger than the others. However, $m_x(t)$ does not show spiking behavior in this IP precession [see the inset of Fig. 2(b)]. Once J_0 exceeds a certain critical value J_c, the auto-oscillation occurs about an OOP precession axis. Figure 2(c) depicts such an OOP precession trajectory for $J_0 = 0.5\,\mathrm{TA/m^2}$. Note that the first harmonic in the corresponding FFT of $m_x(t)$ is shifted toward the higher frequency [see Fig. 2(d)]. This clearly shows the signature of OOP precession mode [43]. In addition, we observe spiking behavior in $m_x(t)$ in this OOP precession mode, as can be seen from the inset of Fig. 2(d). The frequency of the first harmonic varies nonlinearly as a function of the input current density J_0, as depicted in Fig. 2(e). Initially, this frequency decreases to a certain minimum value at $J_0 = 0.465\,\mathrm{TA/m^2}$ and then starts increasing again, indicating the transition from IP to OOP precession. Hence, the critical current for our system is denoted as $J_c = 0.465\,\mathrm{TA/m^2}$. Moreover, we find that the periodicity of the spiking is governed by the first harmonic of the auto-oscillation frequency in the OOP precession mode. It is noteworthy that we did not include any thermal effect to understand the intrinsic magnetization dynamics of our SHNO. However, from a practical perspective, the effect of thermal fluctuation is important to realize the potential for room-temperature operation of such a bias field free SHNO. Hence, we carried out the same simulations at 300 K, considering a random thermal field [42,44]. We observe similar nonlinear behavior of the first harmonic as a function of J_0, although the weaker higher harmonics are suppressed by the thermal noise (see Fig. S1 in the Supplemental Material [45]).

We further observe in Fig. 2(e) that the spiking frequency decreases at a higher value of J_0, as the OOP auto-oscillation trajectory moves away from the $m_z = 0$ plane [see Fig. 2(f)]. However, this leads to generation of better-quality spikes which will be discussed in a later section.

It is important to note that the ellipticity of the FM layer is crucial for the bias-free auto-oscillation of **m**. The elliptic geometry of the FM layer creates a stronger demagnetization field along the minor axis than the major axis due to shape anisotropy. In stable equilibrium, the magnetization prefers alignment close to the major axis (slightly off from the major axis due to $\mathbf{H}_{\mathrm{Oe}}$), as the PMA is not strong enough to fully compensate for the demagnetization field along the film normal. However, when spin current is injected into the FM layer, the SOT attempts to align the magnetization along the spin polarization direction $\mathbf{e}_y$, which coincides with the minor axis. This sets up competition between the SOT and IP demagnetization field that eventually triggers the auto-oscillation of magnetization. To examine the impact of this shape anisotropy on auto-oscillation, we varied the axis ratio of the ellipse while keeping the area constant. This approach ensures a constant total spin-current injection into the FM for a particular value of J_0, regardless of the axis ratio. Figure 3 shows the first harmonic frequency as a function of input current density for different values of axis ratio r. It reveals two key observations: First, the threshold current density increases with increasing axis ratio, and second, the OOP precession is preferred at higher axis ratios. These observations highlight the significant influence of shape anisotropy on the origin and characteristics of auto-oscillation.

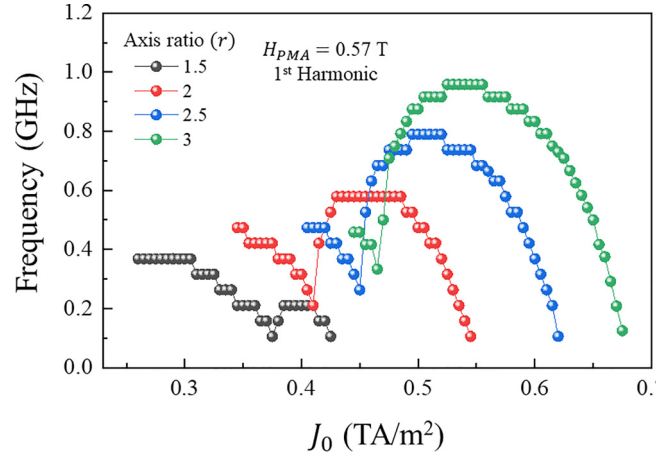

FIG. 3. Variation of the first harmonics of auto-oscillation frequencies as a function of input current density (J_0), for different values of axis ratio (r).

The above results encourage us to gain deeper insight into the origin of bias field free auto-oscillation in our SHNO. However, the microscale physics becomes more complex to understand in the micromagnetic regime. In contrast, the macrospin theory can offer a much simpler model to understand the essential dynamics of the system. In the following section, we investigate the origin of the bias field free auto-oscillation in elliptic SHNO using the macrospin theory.

IV. ORIGIN OF THE BIAS FIELD FREE AUTO-OSCILLATION: MACROSPIN PERSPECTIVE

To understand the origin of bias-free auto-oscillation, we proceed to theoretically calculate the threshold current for exciting the IP auto-oscillation in our system. We employ the macrospin theory along with a linearized Landau-Lifshitz-Gilbert (LLG) equation following the approach of Taniguchi [43] and Taniguchi and Kubota [46]. In the absence of SOT, the orientation of magnetization at stable equilibrium is determined by the minimum energy state. The energy density is given as $E = -M_s \int d\mathbf{m} \cdot \mathbf{H}_{\mathrm{eff}}^{'}$, where $\mathbf{H}_{\mathrm{eff}}^{'} = \mathbf{H}_{\mathrm{Oe}} + \mathbf{H}_{\mathrm{dem}} + \mathbf{H}_{\mathrm{PMA}}$ denotes the effective magnetic field experienced by the magnetization. Hence, the energy density for our system can be written (excluding the constant term) as

$$E = -M_s H_{Oe} \sin\theta \sin\phi - \frac{M_s H_A}{2} \sin^2\theta \cos^2\phi + \frac{M_s H_d}{2} \cos^2\theta. \tag{3}$$

Here, $H_{Oe} = |\mathbf{H}_{\mathrm{Oe}}| = -\mu_0 J_0 t_{HM}/2$, $H_A = \mu_0 M_s (N_y - N_x)$, and $H_d = \mu_0 M_s (N_z - N_y) - H_{\mathrm{PMA}}$.

Note that the demagnetization coefficients N_x, N_y, and N_z are strongly dependent on the axis ratio r (see Fig. 4), as calculated analytically [36]. Here, θ and ϕ in Eq. (3) denote the zenith and azimuthal angle of **m** such that $\mathbf{m} = (\sin\theta\cos\phi, \sin\theta\sin\phi, \cos\theta)$. The minimum energy state ($\mathbf{m} = \mathbf{m}_0$) then corresponds to $\theta = \theta_0 = 90^\circ$ and $\phi = \phi_0 = \sin^{-1}(H_{Oe}/H_A)$, which locates close to the major axis of the ellipse in the xy plane (see the Supplemental Material [45] for derivation). In the presence of spin current, the SOT desta-

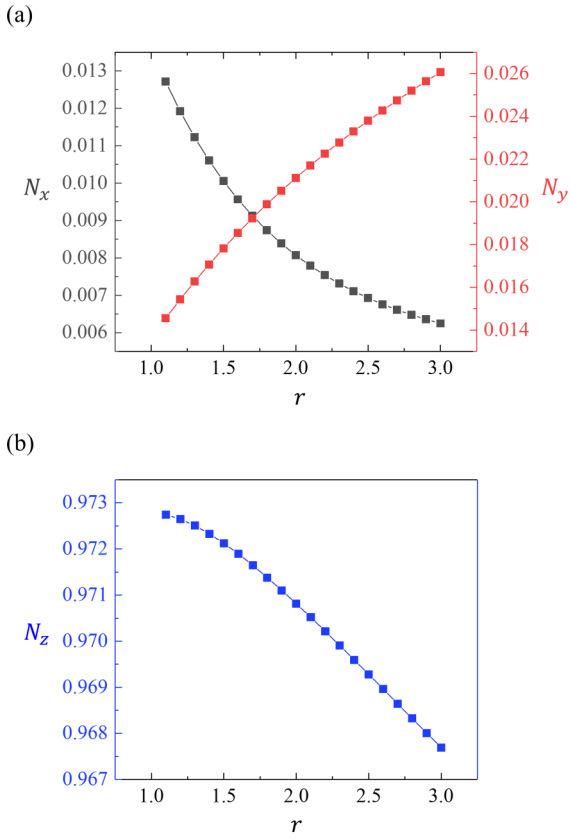

FIG. 4. Variation of the demagnetization coefficients (a) N_x, N_y and (b) N_z along x, y, and z axes, respectively, as a function of axis ratio r.

bilizes the magnetization from the minimum energy state. If the SOT is strong enough to compensate for the damping, it can eventually excite IP auto-oscillation. Assuming a small oscillation amplitude at the onset of magnetization auto-oscillation around the equilibrium stationary point, we can expand the LLG equation around the minimum energy state keeping only the first-order terms in the dynamic $\mathbf{m}(t)$. From such a linearized LLG equation, the instability condition can be extracted as [43]

$$H_{\mathrm{SOT}}(\mathbf{e}_y \cdot \mathbf{m}_0) = \frac{\alpha(H_X + H_Y)}{2}. \tag{4}$$

Here, $H_{\mathrm{SOT}} = \frac{\hbar\theta_{SH} J_0}{2eM_s t_{FM}}$, $H_X = H_{Oe}\sin\phi_0 + H_A\cos^2\phi_0 + H_d$ and $H_Y = H_{Oe}\sin\phi_0 + H_A\cos 2\phi_0$. Now we rewrite $H_{Oe} = -k_1 J_0$ and $H_{\mathrm{SOT}} = k_2 J_0$ for convenience of notation, where $k_1 = \frac{\mu_0 t_{\mathrm{HM}}}{2}$ and $k_2 = \frac{\hbar\theta_{\mathrm{SH}}}{2eM_s t_{\mathrm{FM}}}$. Hence, from Eq. (4), we finally obtain (see the Supplemental Material [45] for the derivation)

$$J_{\mathrm{th}} = \sqrt{\frac{\alpha H_A(2H_A + H_d)}{\alpha k_1^2 - 2k_1 k_2}}. \tag{5}$$

From the above equation, we find that J_{th} will have a real value only if (i) $k_1 \neq 0$, i.e., $H_{Oe} \neq 0$, and (ii) $k_2 < 0$, which implies $\theta_{\mathrm{SH}} < 0$. Hence, we conclude that, firstly, the Oersted field is necessary to achieve the field free oscillation in our system, and secondly, we must choose the HM material with a negative spin Hall angle such as β-W. In fact, without

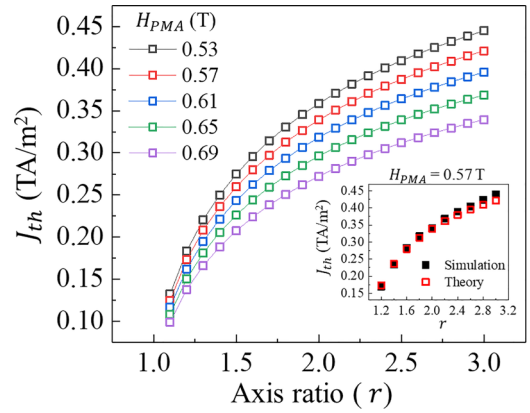

FIG. 5. Variation of the threshold current density (J_{th}) as a function of axis ratio (r), calculated using macrospin theory for different values of perpendicular magnetic anisotropy (PMA) field ($\mathbf{H}_{\mathrm{PMA}}$). (Inset) Comparison of J_{th} calculated analytically using macrospin model and from micromagnetic simulation, for $\mathbf{H}_{\mathrm{PMA}} = 0.57$ T.

the Oersted field, the equilibrium magnetization points along the major axis which is orthogonal to the spin-polarization direction. Therefore, in that case, the SOT cannot destabilize the magnetization. Hence, $\mathbf{H}_{\mathrm{Oe}}$ acts as the symmetry-breaking field in our system.

Figure 5 shows the behavior of J_{th} as a function of r for different values of H_{PMA}. A higher value of the PMA field leads to lower H_d, causing a reduction in J_{th}, as evident from both Eq. (5) and the main plots in Fig. 5. Additionally, the inset of Fig. 5 demonstrates good agreement between the simulated values of J_{th} and those obtained from Eq. (5), confirming the validity of the linearized LLG equation for determining the instability threshold in our system.

V. SPIKING BEHAVIOR OF SHNO

A. IP to OOP transition in the auto-oscillation trajectory

It has been observed [Fig. 2(a)] that the magnetization undergoes bias field free auto-oscillation in IP precession mode if the current density is less than a critical value, denoted by J_c. Above the critical current density, the magnetization precession becomes OOP [Fig. 2(c)]. Additionally, comparing Figs. 2(e) and 3, one can see that J_c is directly dependent on the ellipticity (axis ratio r) of the FM layer. Hence, one might be interested to obtain J_c as a function of r. Note that the linearized LLG equation will no longer be valid because of the large precession amplitude of $\mathbf{m}$. In fact, obtaining a simple analytical expression for J_c as a function of r is practically impossible for our system without the biasing field. The difficulties are well discussed in Ref. [43] and in the Supplemental Material [45]. However, a qualitative picture can be drawn as follows: At a lower value of r, the OOP demagnetization field dominates, which favors IP precession. In contrast, a higher value of r leads to more geometrical confinement along the y axis which results in a higher demagnetization field along the y axis and decrease in the OOP demagnetization field. Therefore, OOP precession is dominant for a higher axis ratio. Hence, from Fig. 3, we observe that the oscillation is mostly IP for $r = 1.5$, whereas the magnetization precession

is predominantly OOP for most of the input current density range in the case of $r = 3$. Additionally, considering only the shape anisotropy and PMA, the macrospin model shows the rate of change in J_c with respect to r, i.e., $\Delta J_c/\Delta r > 0$ (see the Supplemental Material [45]). This is consistent with our micromagnetic simulation results, where J_c increases with r (see Fig. 3).

B. Origin of spiking in OOP precession

We now focus on understanding the spiking behavior in our bias-free SHNO in OOP precession mode. In a SHNO, the sustained precession of magnetization occurs because of the interplay between the energy provided by SOT and the energy dissipation through damping. The work done by SOT (W_{SOT}) and the damping torque (W_α) in a full oscillation cycle are given as [46]

$$W_{\mathrm{SOT}} = \gamma M_s H_{\mathrm{SOT}} \oint [\mathbf{p}\cdot\mathbf{H}_{\mathrm{eff}} - (\mathbf{m}\cdot\mathbf{p})(\mathbf{m}\cdot\mathbf{H}_{\mathrm{eff}})]dt, \quad (6)$$

$$W_\alpha = -\gamma\alpha M_s \oint \left[\mathbf{H}_{\mathrm{eff}}^2 - (\mathbf{m}\cdot\mathbf{H}_{\mathrm{eff}})^2\right]dt. \quad (7)$$

As the input current density exceeds the threshold value, the energy supplied to the magnetization by SOT surpasses the energy dissipation through damping. However, because of the large amplitude precession in our SHNO, the SOT opposes the damping only at certain points on the trajectory of magnetization precession and pumps in power to the oscillatory magnetization. In contrast, the SOT enhances the damping at other points on the precession trajectory, resulting in power loss in the system. This behavior of SOT is directly reflected in the time evolution of the power transferred by SOT ($\frac{dW_{\mathrm{SOT}}}{dt}$) and the power dissipation by intrinsic damping torque ($\frac{dW_\alpha}{dt}$), as shown in Fig. 6(a). Hence, we observe in Fig. 6(a) that $\frac{dW_{\mathrm{SOT}}}{dt}$ (shown in red) is positive for part of the oscillation cycle and negative for the rest of the cycle. Conversely, $\frac{dW_\alpha}{dt}$ (shown in blue) is always negative. We further observe from Fig. 6(a) that the dynamic fluctuation of the power associated with SOT occurs in spiking manner. This can be qualitatively explained considering the interplay of SOT, the Oersted field, and the shape anisotropy due to elliptic geometry of the FM layer. In the auto-oscillation regime of magnetization dynamics, as the SOT orients the magnetization along the spin polarization direction ($\mathbf{e}_y$), the shape anisotropy (along the x axis) and the Oersted field (along $-\mathbf{e}_y$) pull the magnetization away from the spin-polarization direction. The SOT, therefore, keeps on adding more power to the dynamic magnetization to orient it along $\mathbf{e}_y$ again. This leads to acceleration of the magnetization toward $\mathbf{e}_y$ along the precession trajectory. As a result, the SOT draws off power from the dynamic magnetization by enhancing the effective damping and reducing the precessional angular momentum to orient the magnetization along $\mathbf{e}_y$. This cycle repeats again, which leads to the spiking nature of $\frac{dW_{\mathrm{SOT}}}{dt}$.

Figure 6(b) shows the time evolution of the net power available to the system ($\frac{dW_{\mathrm{SOT}}}{dt} + \frac{dW_\alpha}{dt}$) for $J_0 = 0.6\,\mathrm{TA/m^2}$, which follows the time evolution of $\frac{dW_{\mathrm{SOT}}}{dt}$ and fluctuates between negative (net power loss) and positive (net power gain) values throughout the oscillation period. The SOT-driven magnetization precession is, therefore, majorly dictated by the additive or negative power transfer through SOT in a spiking manner. This causes the periodic spiking behavior in the self-oscillatory magnetization dynamics in our SHNO, driven by a constant dc current, as shown in Fig. 6(c).

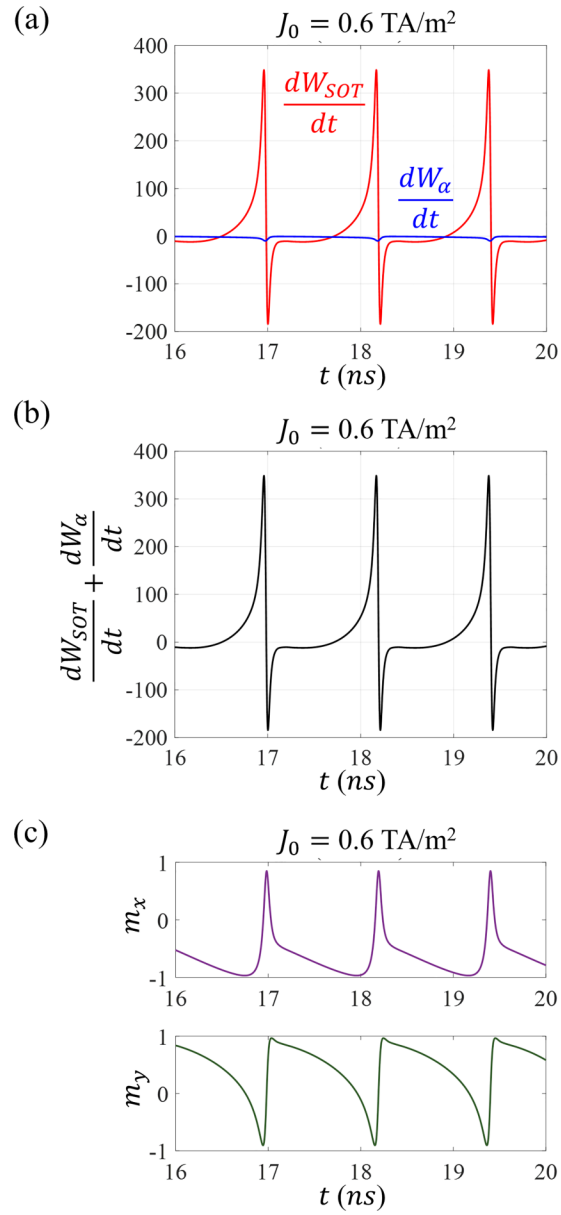

FIG. 6. Dynamics of the power associated with spin-orbit torque (SOT) and damping torque for input current density $J_0 = 0.6\,\mathrm{TA/m^2}$. (a) Time evolution of the power associated with SOT (red) and intrinsic damping torque (blue). (b) Net power available to the system as a function of time (the time independent part is ignored). (c) The corresponding time evolution of m_x and m_y.

C. Tunability of spiking through input current

As mentioned earlier, the spiking occurs in the OOP precession state, with the spiking rate given by the first harmonic extracted from the FFT of m_x. The current tunability of the spiking rate has been shown in Fig. 7(a). During precession, the SOT tries to align $\mathbf{m}$ along the spin-polarization direction

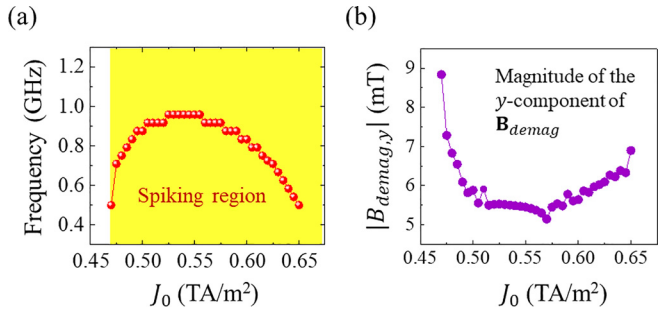

FIG. 7. (a) Variation of spiking rate (first harmonic of auto-oscillation frequency) as a function of input current density J_0 in out-of-plane (OOP) precession mode. This shows the current tunability of spiking rate. (b) Variation of the magnitude of y component of demagnetization field $\mathbf{B}_{\text{demag}}$ as a function of J_0.

$\mathbf{e}_y$, which is opposed by the demagnetization field along the y axis. Hence, a stronger demagnetization field along the y axis makes $\mathbf{m}$ move faster to pass the $\mathbf{e}_y$ direction. Conversely, a lower value of the demagnetization field along the y axis allows $\mathbf{m}$ to stay oriented along $\mathbf{e}_y$ for a longer duration, resulting in a lower auto-oscillation frequency and spiking rate. Figure 7(b) shows the variation of the time-averaged y component of demagnetization field, which is opposite to the behavior of spiking rate shown in Fig. 7(a).

The bias field free SHNO exhibits not only current tunability of the spiking rate but also improved spike sharpness with higher input current density. As shown in Fig. 2(f), at higher input current, the precession trajectory becomes more OOP. Figure 8 illustrates the variation of the time-averaged value of θ', where $\theta' = 180^\circ - \theta$, measured from the $-$z axis (see the inset of Fig. 8), as a function of input current density. Spiking in $m_x(t)$ for certain values of time-averaged θ' are also shown in Fig. 8. Note that, as θ' becomes relatively smaller, i.e., $\mathbf{m}$ moves closer to the $-$z axis at higher input current, sharper

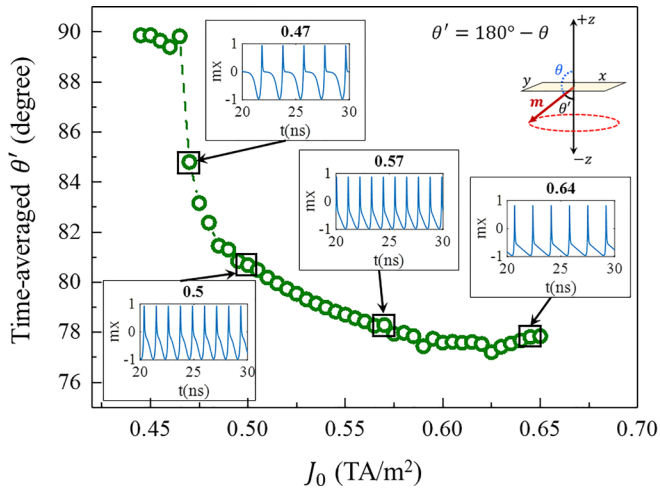

FIG. 8. Variation of the time-averaged value of the out-of-plane angle θ' (measured from the $-$z axis) as a function of input current density J_0. Sharper spikes are obtained at higher current density and lower value of θ'. This indicates the current tunability of spiking rate and quality.

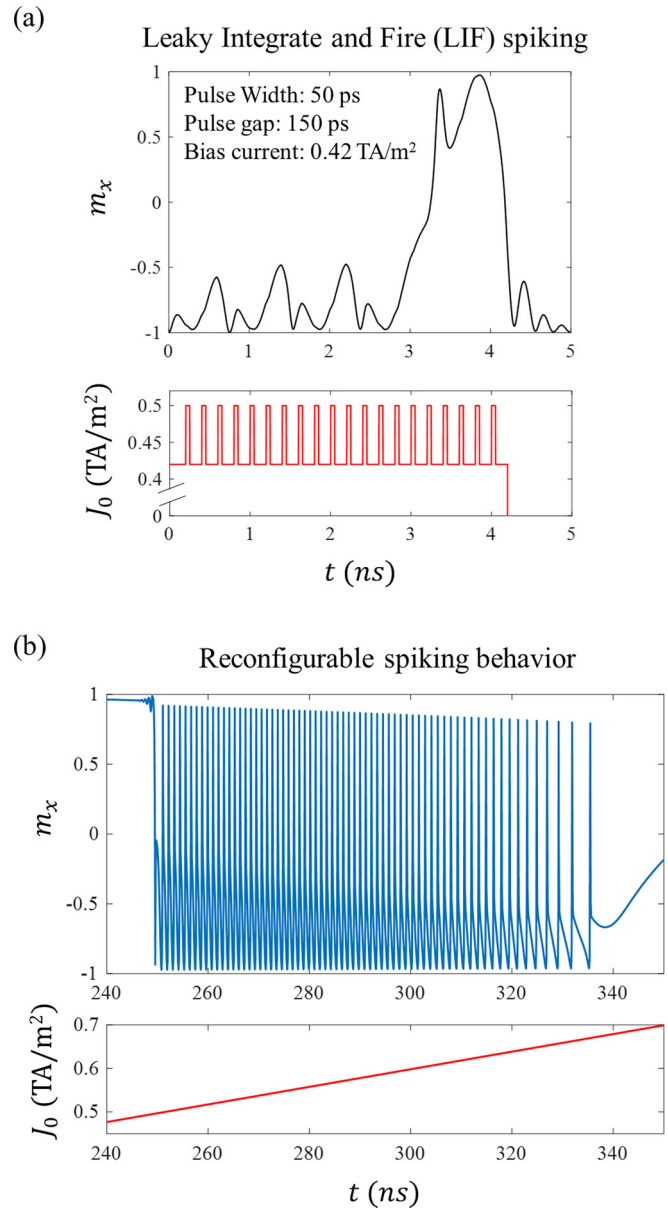

FIG. 9. (a) Leaky integrate-and-fire (LIF) behavior in a spin Hall nano-oscillator (SHNO) in the presence of consecutive excitatory pulses along with a constant bias current. (b) Reconfigurable spiking behavior in SHNO in the presence of a linearly varying input current density. At relatively higher values of current density, the spiking rate and quality are self-adjusted based on the value of input current density.

spikes are generated. This highlights the tunability of spike quality by varying the input current.

Finally, we demonstrate LIF and reconfigurable spiking behavior in our bias field free SHNO. In the LIF neuron model, the consecutive input excitatory pulses gradually increase the membrane potential, while it decreases (leaks) in the absence of the excitatory pulses. After a certain number of consecutive input excitatory pulses, the membrane potential surpasses a threshold, and the neuron fires. Similar behavior has been obtained in our SHNO when it is excited by consecutive subnanosecond current pulses in the presence of

a constant biasing current density less than J_{th}. Figure 9(a) depicts this LIF behavior of our SHNO. Note that the firing threshold is achieved when the m_x value is slightly >0.5. This LIF behavior highlights the potential of such a bias field free SHNO for neuromorphic computing applications such as image recognition using SNN [47]. In Fig. 9(b), we show the reconfigurable spiking behavior of our SHNO upon excitation by a linearly varying input current density. In a SNN, reconfigurable spiking neurons are designed to dynamically adapt to the variation in input and adjust their properties during runtime. As shown in Fig. 9(b), our bias field free SHNO exhibits on-the-fly variation in spiking rate, amplitude, and sharpness in response to varying input current density. This adaptability would allow the SHNO to efficiently process time-varying and event-based data, enhancing its flexibility and performance with changing inputs. However, this reconfigurability is accomplished mostly at higher input currents, as seen in Fig. 9(b). Both behaviors strongly suggest the potential of such a bias-free SHNO in designing efficient neuromorphic hardware with spiking neurons.

VI. CONCLUSIONS

In conclusion, in this paper, we unveil intriguing insight into the behavior of a bias field free SHNO with simple elliptic geometry and its potential applications in designing artificial neurons for SNN-based neuromorphic hardware. In addition to the bias field free auto-oscillation of magnetization, a current-tunable transition from IP to OOP precession mode is achieved. In the OOP precession mode, the elliptic SHNO exhibits neuronlike spiking dynamics which can be modulated in terms of spiking rate and sharpness through adjustments in input dc current. Notably, we observed both periodic and LIF spiking behavior in the same SHNO device, achievable by manipulating the pulse width and amplitude of the input dc current. Furthermore, the large precession amplitude ensures that the output spike signals are sufficiently strong for efficient signal processing. Our discussion on the impact of geometrical parameters on determination of auto-oscillation characteristics will help to optimize the geometry in a much more efficient way for greater scalability. Therefore, this paper can motivate further exploration of the potential of bias field free SHNOs in next-generation computing and information processing paradigms.

The data that support the findings of this paper are available from the corresponding author upon reasonable request.

ACKNOWLEDGMENTS

S.M. would like to acknowledge the NTU-Research Scholarship (NTU-RSS). R.S.R. acknowledges the research project support by the Ministry of Education (MOE), Singapore, under its Academic Research Fund Tier 1 (Grant No.: RG76/22). Any opinions, findings and conclusions, or recommendations expressed in this material are those of the author(s) and do not reflect the views of the Ministry of Education, Singapore. R.M. would like to acknowledge the Initiation Grant, IIT Kanpur, and I-HUB Quantum Technology Foundation, IISER Pune for Financial support.

[1] J. Grollier, D. Querlioz, K. Y. Camsari, K. Everschor-Sitte, S. Fukami, and M. D. Stiles, Neuromorphic spintronics, Nat. Electron. **3**, 360 (2020).

[2] D. V. Christensen, R. Dittmann, B. Linares-Barranco, A. Sebastian, M. Le Gallo, A. Redaelli, S. Slesazeck, T. Mikolajick, S. Spiga, S. Menzel *et al.*, 2022 roadmap on neuromorphic computing and engineering, Neuromorph. Comput. Eng. **2**, 022501 (2022).

[3] T. Taniguchi, S. Tsunegi, S. Miwa, K. Fujii, H. Kubota, and K. Nakajima, in *Reservoir Computing: Theory, Physical Implementations, and Applications*, edited by K. Nakajima and I. Fischer (Springer, Singapore, 2021), p. 331.

[4] F. C. Hoppensteadt and E. M. Izhikevich, Oscillatory neurocomputers with dynamic connectivity, Phys. Rev. Lett. **82**, 2983 (1999).

[5] T. Aonishi, K. Kurata, and M. Okada, Statistical mechanics of an oscillator associative memory with scattered natural frequencies, Phys. Rev. Lett. **82**, 2800 (1999).

[6] R. Matsumoto, S. Lequeux, H. Imamura, and J. Grollier, Chaos and relaxation oscillations in spin-torque windmill spiking oscillators, Phys. Rev. Appl. **11**, 044093 (2019).

[7] J. Torrejon, M. Riou, F. A. Araujo, S. Tsunegi, G. Khalsa, D. Querlioz, P. Bortolotti, V. Cros, K. Yakushiji, A. Fukushima *et al.*, Neuromorphic computing with nanoscale spintronic oscillators, Nature **547**, 428 (2017).

[8] M. Zahedinejad, A. A. Awad, S. Muralidhar, R. Khymyn, H. Fulara, H. Mazraati, M. Dvornik, and J. Akerman, Two-dimensional mutually synchronized spin Hall nano-oscillator arrays for neuromorphic computing, Nat. Nanotechnol. **15**, 47 (2020).

[9] M. Zahedinejad, H. Fulara, R. Khymyn, A. Houshang, M. Dvornik, S. Fukami, S. Kanai, H. Ohno, and J. Akerman, Memristive control of mutual spin Hall nano-oscillator synchronization for neuromorphic computing, Nat. Mater. **21**, 81 (2022).

[10] D. I. Albertsson, M. Zahedinejad, A. Houshang, R. Khymyn, J. Åkerman, and A. Rusu, Ultrafast Ising machines using spin torque nano-oscillators, Appl. Phys. Lett. **118**, 112404 (2021).

[11] A. Houshang, M. Zahedinejad, S. Muralidhar, J. Checinski, R. Khymyn, M. Rajabali, H. Fulara, A. A. Awad, M. Dvornik, and J. Akerman, Phase-binarized spin Hall nano-oscillator arrays: Towards spin Hall Ising machines, Phys. Rev. Appl. **17**, 014003 (2022).

[12] A. J. Mathew, J. R. Mohan, R. Feng, R. Medwal, S. Gupta, R. S. Rawat, and Y. Fukuma, Evaluation of memory capacity and time series prediction using a spin Hall oscillator as reservoir, IEEE Trans. Magn. **59**, 1 (2023).

[13] J. R. Mohan, A. J. Mathew, K. Nishimura, R. Feng, R. Medwal, S. Gupta, R. S. Rawat, and Y. Fukuma, Classification tasks using input driven nonlinear magnetization dynamics in spin Hall oscillator, Sci. Rep. **13**, 7909 (2023).

[14] D. R. Rodrigues, R. Moukhader, Y. Luo, B. Fang, A. Pontlevy, A. Hamadeh, Z. Zeng, M. Carpentieri, and G. Finocchio, Spintronic Hodgkin-Huxley-analogue neuron implemented with a single magnetic tunnel junction, Phys. Rev. Appl. **19**, 064010 (2023).

[15] R. Khymyn, I. Lisenkov, V. Tiberkevich, B. A. Ivanov, and A. Slavin, Antiferromagnetic THz-frequency Josephson-like oscillator driven by spin current, Sci. Rep. **7**, 43705 (2017).

[16] H. Bradley, S. Louis, C. Trevillian, L. Quach, E. Bankowski, A. Slavin, and V. Tyberkevych, Artificial neurons based on antiferromagnetic auto-oscillators as a platform for neuromorphic computing, AIP Advances **13**, 015206 (2023).

[17] F. J. T. Gonçalves, T. Hache, M. Bejarano, T. Hula, O. Hellwig, J. Fassbender, and H. Schultheiss, Agility of spin Hall nano-oscillators, Phys. Rev. Appl. **16**, 054050 (2021).

[18] T. Hache, L. Körber, T. Hula, K. Lenz, A. Kákay, O. Hellwig, J. Lindner, J. Fassbender, and H. Schultheiss, Control of four-magnon scattering by pure spin current in a magnonic waveguide, Phys. Rev. Appl. **20**, 014062 (2023).

[19] J. E. Hirsch, Spin Hall effect, Phys. Rev. Lett. **83**, 1834 (1999).

[20] V. E. Demidov, S. Urazhdin, A. Zholud, A. V. Sadovnikov, and S. O. Demokritov, Nanoconstriction-based spin-Hall nano-oscillator, Appl. Phys. Lett. **105**, 172410 (2014).

[21] A. A. Awad, P. Dürrenfeld, A. Houshang, M. Dvornik, E. Iacocca, R. K. Dumas, and J. Åkerman, Long-range mutual synchronization of spin Hall nano-oscillators, Nat. Phys. **13**, 292 (2016).

[22] A. A. Awad, A. Houshang, M. Zahedinejad, R. Khymyn, and J. Åkerman, Width dependent auto-oscillating properties of constriction based spin Hall nano-oscillators, Appl. Phys. Lett. **116**, 232401 (2020).

[23] P. Durrenfeld, A. A. Awad, A. Houshang, R. K. Dumas, and J. Akerman, A 20 nm spin Hall nano-oscillator, Nanoscale **9**, 1285 (2017).

[24] H. Fulara, M. Zahedinejad, R. Khymyn, A. A. Awad, S. Muralidhar, M. Dvornik, and J. Åkerman, Spin-orbit torque–driven propagating spin waves, Sci. Adv. **5**, eaax8467 (2019).

[25] H. Fulara, M. Zahedinejad, R. Khymyn, M. Dvornik, S. Fukami, S. Kanai, H. Ohno, and J. Akerman, Giant voltage-controlled modulation of spin Hall nano-oscillator damping, Nat. Commun. **11**, 4006 (2020).

[26] A. Kumar, M. Rajabali, V. H. Gonzalez, M. Zahedinejad, A. Houshang, and J. Akerman, Fabrication of voltage-gated spin Hall nano-oscillators, Nanoscale **14**, 1432 (2022).

[27] H. Mazraati, S. Muralidhar, S. R. Etesami, M. Zahedinejad, S. A. H. Banuazizi, S. Chung, A. Awad, R. Khymyn, M. Dvornik, and J. Akerman, Mutual synchronization of constriction-based spin Hall nano-oscillators in weak in-plane magnetic fields, Phys. Rev. Appl. **18**, 014026 (2022).

[28] B. Jiang, W. Zhang, J. Li, S. Yu, G. Han, S. Xiao, G. Liu, S. Yan, and S. Kang, Terahertz spectrum in SHNO driven by the pure spin current, AIP Advances **10**, 015126 (2020).

[29] B. Jiang, W. Zhang, H. Zhong, Y. Zhang, S. Yu, G. Han, S. Xiao, G. Liu, S. Yan, J. Li, and S. Kang, Towards terahertz spin Hall nano-oscillator with synthesized anti-ferromagnets, J. Magn. Magn. Mater. **490**, 165470 (2019).

[30] S. Manna, R. Medwal, S. Gupta, J. R. Mohan, Y. Fukuma, and R. S. Rawat, Anisotropy-assisted bias-free spin Hall nano-oscillator, Appl. Phys. Lett. **122**, 072401 (2023).

[31] T. Shirokura and P. N. Hai, Bias-field-free spin Hall nano-oscillators with an out-of-plane precession mode, J. Appl. Phys. **127**, 103904 (2020).

[32] D. Marković, M. W. Daniels, P. Sethi, A. D. Kent, M. D. Stiles, and J. Grollier, Easy-plane spin Hall nano-oscillators as spiking neurons for neuromorphic computing, Phys. Rev. B **105**, 014411 (2022).

[33] A. L. Hodgkin and A. F. Huxley, A quantitative description of membrane current and its application to conduction and excitation in nerve, J. Physiol. **117**, 500 (1952).

[34] D. Wang, R. Tang, H. Lin, N. Xu, Y. Sun, X. Zhao, Z. Wang, D. Wang, Z. Mai, Y. Zhou *et al.*, Spintronic leaky-integrate-fire spiking neurons with self-reset and winner-takes-all for neuromorphic computing, Nat. Commun. **14**, 1068 (2023).

[35] X. Liang, X. Zhang, J. Xia, M. Ezawa, Y. Zhao, G. Zhao, and Y. Zhou, A spiking neuron constructed by the Skyrmion-based spin torque nano-oscillator, Appl. Phys. Lett. **116**, 122402 (2020).

[36] M. Beleggia, M. D. Graef, Y. T. Millev, D. A. Goode, and G. Rowlands, Demagnetization factors for elliptic cylinders, J. Phys. D Appl. Phys. **38**, 3333 (2005).

[37] W. Skowroński, L. Karwacki, S. Zietek, J. Kanak, S. Lazarski, K. Grochot, T. Stobiecki, P. Kuswik, F. Stobiecki, and J. Barnas, Determination of spin Hall angle in heavy-metal/Co-Fe-B based heterostructures with interfacial spin-orbit fields, Phys. Rev. Appl. **11**, 024039 (2019).

[38] R. Bansal, G. Nirala, A. Kumar, S. Chaudhary, and P. K. Muduli, Large spin Hall angle in β-W thin films grown on CoFeB without oxygen plasma, SPIN **08**, 1850018 (2018).

[39] Y.-C. Lau and M. Hayashi, Spin torque efficiency of Ta, W, and Pt in metallic bilayers evaluated by harmonic Hall and spin Hall magnetoresistance measurements, Jpn. J. Appl. Phys. **56**, 0802B5 (2017).

[40] J. C. Slonczewski, Current-driven excitation of magnetic multilayers, J. Magn. Magn. Mater. **159**, L1 (1996).

[41] L. Liu, T. Moriyama, D. C. Ralph, and R. A. Buhrman, Spin-torque ferromagnetic resonance induced by the spin Hall effect, Phys. Rev. Lett. **106**, 036601 (2011).

[42] A. Vansteenkiste, J. Leliaert, M. Dvornik, M. Helsen, F. Garcia-Sanchez, and B. Van Waeyenberge, The design and verification of MuMax^3, AIP Advances **4**, 107133 (2014).

[43] T. Taniguchi, Out-of-plane magnetization oscillation in spin Hall device assisted by field-like torque, Appl. Phys. Lett. **118**, 142406 (2021).

[44] J. Leliaert, J. Mulkers, J. De Clercq, A. Coene, M. Dvornik, and B. Van Waeyenberge, Adaptively time stepping the stochastic Landau-Lifshitz-Gilbert equation at nonzero temperature: Implementation and validation in MuMax^3, AIP Advances **7**, 125010 (2017).

[45] See Supplemental Material at http://link.aps.org/supplemental/10.1103/PhysRevB.108.184411 for the detailed methodology of micromagnetic simulation, effect of finite temperature, derivation of the threshold current using macrospin model, and a note on the analytical derivation of the critical current density, which also includes Refs. [36,43,46].

[46] T. Taniguchi and H. Kubota, Instability analysis of spin-torque oscillator with an in-plane magnetized free layer and a perpendicularly magnetized pinned layer, Phys. Rev. B **93**, 174401 (2016).

[47] E. Doutsi, L. Fillatre, M. Antonini, and P. Tsakalides, Dynamic image quantization using leaky integrate-and-fire neurons, IEEE Trans. Image Process. **30**, 4305 (2021).